

Micro and nanolattice fabrication using projection micro litho stereo exposure additive manufacturing techniques and synchrotron X-ray 3D imaging-based defect characterization

HU WenXia¹, LIU LiWu², WU WenWang^{1,4*}, XI Li^{1*}, LENG JinSong³ & FANG DaiNing¹¹ Institute of Advanced Structure Technology, Beijing Institute of Technology, Beijing 100081, China;² Department of Astronautical Science and Mechanics, Harbin Institute of Technology, Harbin 150001, China;³ National Key Laboratory of Science and Technology on Advanced Composites in Special Environments, Harbin Institute of Technology (HIT), Harbin 150080, China;⁴ Department of Mechanical Engineering, Massachusetts Institute of Technology, Cambridge MA 02139, USA

Received July 15, 2019; accepted September 24, 2019; published online March 3, 2020

Synchrotron radiation X-ray micro-computed tomography (SR- μ CT) is a 3D imaging technique that is widely employed for the characterization of defects in advanced materials and structures. In this study, we characterize several typical defects in octet-truss and re-entrant 3D lattice structures by using SR- μ CT. The 3D micro-lattice structures are manufactured using projection micro litho stereo exposure (P μ LSE) additive manufacturing technology. The as-fabricated 3D lattice samples are characterized using optical microscopy, and subsequently, by SR- μ CT. Further more, a statistical analysis is performed to characterize the surface roughness and internal defects qualitatively, whereby the statistical geometrical parameters of struts along different directions and strut joints are analyzed and classified. Consequently, several typical defects are identified: (1) holes at the joints of the strut and irregular diameter deviations of the strut in the octet-truss lattice structure; (2) irregular diameter variations, bulges, dislocations, grooves, accumulations, and torsion in the re-entrant lattice structure. All of these defects are related to the building direction, the weight of the structure, bubbles, dust, and impurities during the P μ LSE additive manufacturing process.

synchrotron radiation X-ray, additive manufacturing, lattice structures, defect characterization

Citation: Hu W X, Liu L W, Wu W W, et al. Micro and nanolattice fabrication using projection micro litho stereo exposure additive manufacturing techniques and synchrotron X-ray 3D imaging-based defect characterization. *Sci China Tech Sci*, 2020, 63: 561–570, <https://doi.org/10.1007/s11431-019-1453-4>

1 Introduction

Auxetic materials expand transversely when subjected to tension in the longitudinal direction, and contract transversely when subjected to compression in the longitudinal direction [1,2]. Furthermore, compared to traditional materials, auxetic materials and structures have superior impact resistance, shear resistance, sound absorption, and vibration absorption, etc. Owing to their robust multifunctional mechanical performances, auxetic materials are expected to be

used in textile, aerospace, biomedical, and smart sensor industries.

3D printing at the micro and nano scales has potential for industrial application in manufacturing micro-nano electro-mechanical systems, biomedicines [3,4], micro-nano sensors, micro-nano electronics, biochips, optoelectronics [5], and micro fluidic devices. In recent years, projection micro litho stereo exposure (P μ LSE) additive manufacturing technology has been considered as one of the most promising micro-machining technologies, demonstrating great advantages in speed, spatial resolution, and cost.

Owing to the limitations of manufacturing process, various

*Corresponding authors (email: wuw05@mit.edu; xili@bit.edu.cn)

types of surface and internal defects are inevitable in as-fabricated lattice mechanical metamaterials prepared by micro/nano additive manufacturing techniques. To improve the manufacturing process and maintain the mechanical integrity of the products, it is important to assess the manufacturing defects quantitatively and analyze the relation between defects and mechanical performances of the final as-fabricated metamaterials. Synchrotron radiation X-ray micro-computed tomography (SR- μ CT) is a non-destructive 3D imaging technique, which can be used for characterizing the internal 3D defects in advanced materials and structures, and has been widely employed in the aerospace, automobile, energy, electronics, and additive manufacturing industries. Kim et al. [6] outlined the application of micro-computed tomography as a through-process quantification tool for characterizing internal pore, strut size, variation features, and tracking morphological changes during the manufacturing process. Kerckhofs et al. [7] proposed a novel method to quantify the surface roughness of 3D additive-manufactured porous structures based on high-resolution micro-computed tomography. Song et al. [8] compounded a novel high-entropy alloy-coated nano lattice composite material, and studied its mechanical performance based on progressive damage theory and damage mechanics. Using synchrotron X-ray tomography 3D imaging, Scarlett et al. [9,10] analyzed the external morphology, dimension precision, and internal defects of titanium parts fabricated by additive manufacturing. Uesugi et al. [11] investigated the microstructures and defects of 3D carbonaceous chondrites based on SR-CT and identified their chemical composition by interpreting the linear attenuation coefficient through X-ray images. Fan et al. [12] investigated the effect of the tensile stress on the crystallization and average grain size of a Fe-CuNbSiB amorphous alloy using an *in-situ* synchrotron radiation X-ray diffraction technique. By analyzing the morphology using *in-situ* compression tomography, Liu et al. [13] investigated the effects of defects locations and spatial distribution on the elastic response, damage initiation, and failure evolution of 3D metallic lattice samples under quasi-static compression. Using SR- μ CT technique, Hu et al. [14] studied the effects of micro structural features on the me-

chanical properties of hybrid laser-welded 7020-T651 aluminum alloys, such as fatigue strength and damage mechanism. Using SR- μ CT-reconstructed microstructure information, Wu et al. [15] analyzed the effect of microstructures and gas pores on the fatigue behavior and performance of hybrid laser-welded high-Zn 7000 series Al-alloys through a finite element analysis. Wu et al. [16] reviewed the applications of *in-situ* SR- μ CT technique for the investigation of internal damage accumulation and defect evolution processes of various types of advanced-structure materials, including the complex interaction between cracks and pores, precipitates, inter metallic inclusions, and grains. Wu et al. [17] investigated the mechanical performance and 3D failure mechanism maps of a pyramidal-pyramidal hierarchical lattice material under different loading conditions. Xu et al. [18] investigated the effect of different printing directions of a 3D printer on the mechanical properties of lattice elements by uniaxial tensile tests.

These studies show that SR- μ CT is suitable for the characterization of surface roughness and internal defects, such as holes, cracks, and bulges in advanced materials and structures that cannot be directly observed by 2D optical microscopy. In this study, SR- μ CT 3D image reconstruction and optical microscopy are used to characterize the defects of octet-truss and re-entrant lattice structures manufactured with P μ LSE 3D printing, as shown in Figure 1. Further, the surface topography, internal defects, and cross-section profile of the strut are analyzed statically, and typical defects types are classified. Subsequently, the relations between the additive manufacturing process and typical defects are explored, and it is found that the defects are related to the building direction, the weight of the structure, and the bubbles and impurities that are introduced during the manufacturing process.

2 Mechanical design and manufacturing

2.1 Design model of lattice structures

The geometric models of the 3D octet-truss and re-entrant lattice structures are shown in Figure 2. Figure 2(a) and (b)

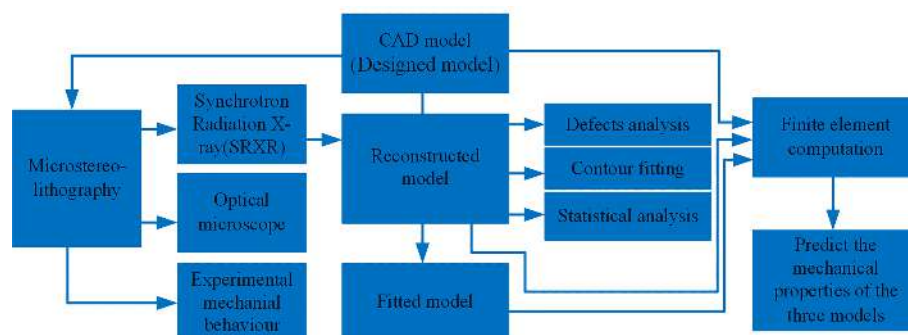


Figure 1 (Color online) Flowchart of the lattice fabrication and defect characterization processes.

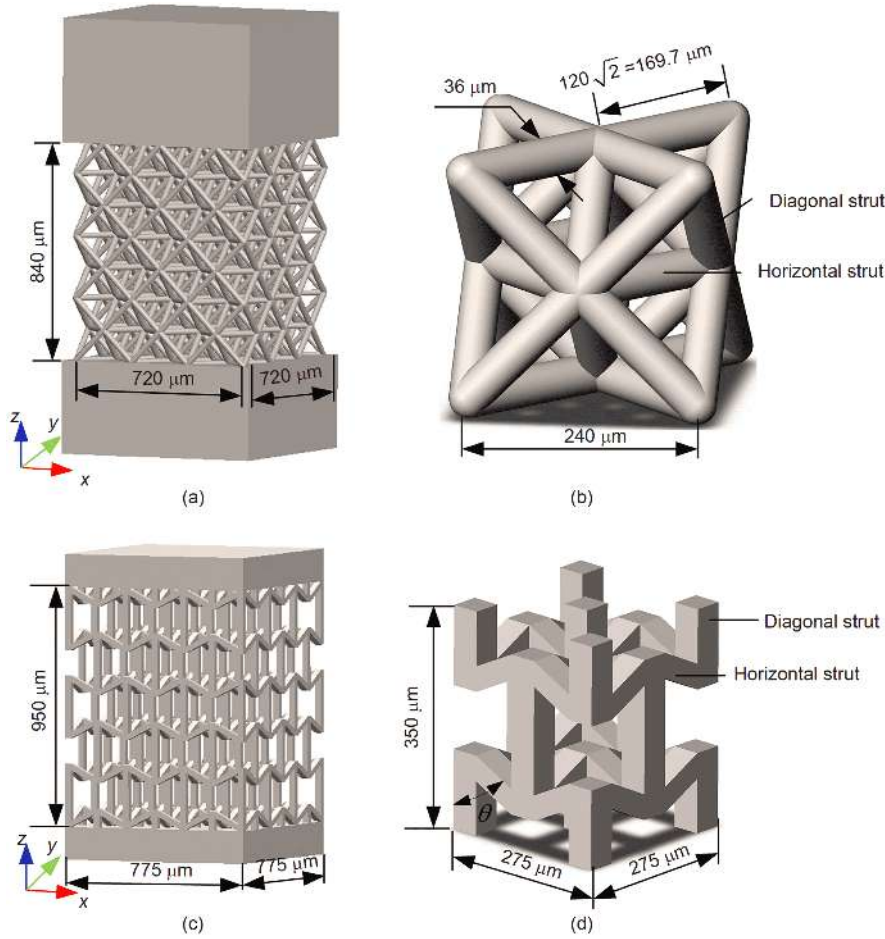


Figure 2 (Color online) Ideal model. (a) octet-truss lattice structure (sample 1); (b) re-entrant lattice structure (sample 2); (c) unit cell of sample 1; (d) unit cell of sample 2.

shows the octet-truss lattice structure (which is referred as sample 1 in this paper) and its unit cell, respectively. The struts are categorized into two types: horizontal (perpendicular to the z -axis) and diagonal (45.0° relative to the z -axis). **Figure 2(c)** and **(d)** shows the re-entrant lattice structure (which is referred to as sample 2 in this paper) and its unit cell, respectively. As shown in **Figure 2**, all unit cells have cubic symmetry, the cross section of the strut for the sample 1 is a circle, and the diameter of the strut is $36 \mu\text{m}$. For sample 2, the cross section of the strut is a square with a side length of $45 \mu\text{m}$. Depending on the angle between the rod and the z -axis, the strut can be vertical (parallel to the z -axis) and diagonal (63.4° relative to the z -axis).

The relative density $\bar{\rho}$ of the lattice structure is equal to the ratio of the macroscopic density ρ of the cellular structure to the density ρ_s of the structure's material, as follows [19]:

$$\bar{\rho} = \frac{\rho}{\rho_s}. \quad (1)$$

The relative density and compressive stiffness of the ideal octet-truss lattice structure [20,21] are given by

$$\bar{\rho} = 6\sqrt{2}\pi\left(\frac{r}{l}\right)^2\left(1 - \frac{r}{l}\left(\sqrt{2} + \frac{2}{\pi}\right)\right), \quad (2)$$

$$E = \frac{\bar{\rho}}{9\left(1 - \frac{r}{l}\left(\sqrt{2} + \frac{2}{\pi}\right)\right)^2}\left(1 + \frac{8K_2}{3 + K_2}\right), \quad (3)$$

where r and l represent the radius and length of the strut, respectively. $K_2 = 3K_1(r/l_c)^2$ is the coupling coefficient of the strut, where

$$K_1 = 1 / \left(1 + 12E_s I / G\kappa A l_c^2\right), \quad (4)$$

where G is the shear modulus of the strut material, κ is the shear coefficient ($\kappa = 0.9$ for a circular beam), I is the moment of inertia of the beam, given by $\pi r^4/4$ for a circular cross section, E_s is the elastic modulus of strut material, and A is the cross-sectional area of the strut, given by πr^2 . Finally, l_c is the effective length of the strut, given by

$$l_c = \left[1 - \left(\sqrt{2} + \frac{2}{\pi}\right)\frac{r}{l}\right]. \quad (5)$$

The relative density of the ideal re-entrant lattice structure [22] is obtained as follows:

$$\bar{\rho} = \frac{t^2(H+4L)}{2l^2\sin^2\theta(k-l\cos\theta)}, \quad (6)$$

where $H = k + \frac{t(1-\cos\theta)}{\sin\theta}$, $L = \left(l - \frac{t}{\sin\theta}\right)$, with t , l , and k being the side lengths of the strut cross section, the length of the re-entrant strut, and length of the vertical strut, respectively. θ is the re-entrant angle between the oblique and vertical struts.

The Poisson's ratio and the effective modulus in the z direction under compressive stress can be written as follows [23]:

$$\nu_{zx} = \frac{-5\cos\theta(GL^2+6Et)(\alpha-\cos\theta)}{(L^2+6t^2)\sin^2\theta+4\alpha t^4}, \quad (7)$$

$$E_z = \frac{\frac{t^2(k-l\cos\theta)}{l^2\sin^2\theta}}{(l-2\Delta l)\sin^2\theta\left(\frac{(l-2\Delta l)^2}{2E_s t^2} + \frac{3}{5G_s}\right) + \frac{(l-2\Delta l)\cos^2\theta+2(k-2\Delta k)}{2E_s}}. \quad (8)$$

2.2 Fabrication of lattice samples

The lattice samples are fabricated by high-precision PμLSE with the nanoArch® S130 3D printing system (BMF R Precision Technology Co, Ltd, Shenzhen, China). The materials employed for printing are photosensitive resin poly (ethylene glycol) diacrylate, PEGDA (BMF Material Technology Inc.). The fabrication sample resolution is 2 μm, and a 405 nm LED light source is employed for generating a light intensity of 45 mW/cm², and the exposure time is 1 s. After being printed, the harvested raw lattice sample is cleaned with isopropyl alcohol (IPA) for 30 s to dissolve the residual liquid resin off the lattice sample. Then, the lattice is dried in an oven at 50°C for 10 min, and irradiation with UV light at a 35 mW/cm² intensity is employed for final solidification of lattice sample.

3 Tomography experiments and defects analysis

Surface and internal defects of micro lattice structures are inevitable in the as-fabricated samples, and these defects will influence the mechanical properties and integrity of the lattice structures. In this study, the surface and internal structures of the octet-truss and re-entrant lattice structures are characterized by optical microscopy and SR-μCT, respectively. The advantage of optical microscopy is that it can clearly characterize the surface topography. However, the

detailed internal structures cannot be characterized. Thus, the 3D surface topography and internal defects of the lattice structure are analyzed using SR-μCT.

3.1 Optical microscopy characterization

The images of the octet-truss and re-entrant lattice structure obtained using optical microscopy are shown in Figure 3. The octet-truss lattice structure consists of stacked structures on the diagonal strut and holes at the joints of the strut. Figure 3(a) shows that the joints of the struts are thicker than that of the ideal structure. The strut stacking and strut thickness heterogeneity represent a mismatch between the design and the manufactured samples. These defects will have a substantial impact on the mechanical properties of the octet-truss lattice structure, such as stress concentration. These thickened joints are caused by some factors involved with PμLSE additive manufacturing process and complex chemical-mechanical solidification process.

It is seen that the strut surface of the 3D re-entrant lattice structure looks smoother than that of the octet-truss lattice structure, and no stacked structure is observed. However, as can be seen from Figure 3(b)–(c), the thickness of the vertical struts changes gradually from the middle point of the strut to the joint node position; furthermore, the two ends of the vertical strut (I and III) are thicker than the middle of the strut (II), and the thickness of strut V is significantly different from that of strut VI.

3.2 Synchrotron radiation X-ray 3D imaging technique

SR-μCT 3D imaging experiments were performed at the Shanghai Synchrotron Radiation X-ray facility on the BL13W1 beamline for characterizing the imperfections of the octet-truss and re-entrant lattice structures. The X-ray beam energy was 18 keV, the pixel size was 0.65 μm, the distance between the sample and the detector was 0.1, and the exposure time was 500 ms. During the experiments, the specimen was rotated 180° along the vertical direction with 0.25° increments. A flowchart of the process used for harvesting 3D X-ray images via image reconstruction is shown in Figure 4. The AvizoR software was employed for 3D visualization and analysis, which included the following steps: process image filtering, image segmentation, 3D visualization, materials characterization, and quantitative analysis.

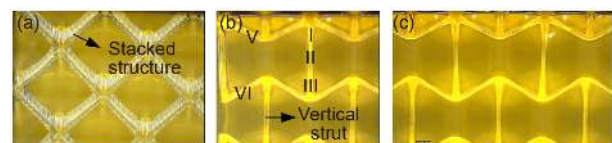


Figure 3 (Color online) Optical microscopy images of (a) yz view of octet-truss lattice structure; (b) yz view of re-entrant lattice structure; (c) xz view of re-entrant lattice structure.

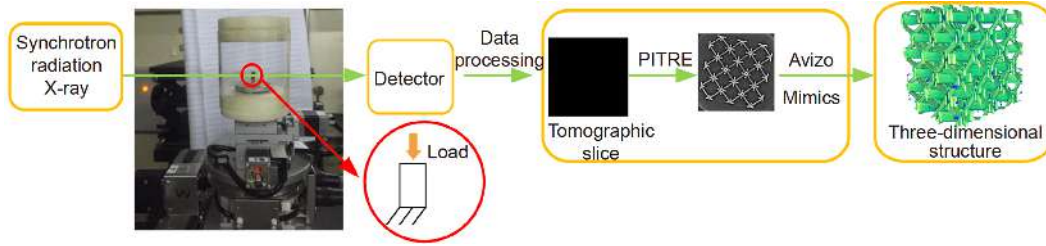


Figure 4 (Color online) Flowchart of the 3D X-ray imaging and tomography reconstruction process.

3.3 Image processing (3D reconstruction) and defects analysis

The raw images were obtained using SR- μ CT 3D imaging and were processed using the AvizoR software to obtain a 3D reconstructed geometric model. The steps involved in the 3D reconstruction process were as follows: slice processing, threshold optimization, image segmentation, and 3D reconstruction.

3.3.1 Reconstruction and defect analysis for octet-truss lattice structure

The reconstructed 3D geometric model of the octet-truss structure is shown in Figure 5(a). It can be seen that the cross section of the horizontal struts of the octet-truss lattice structure exhibits a waterdrop shape and has a smooth surface that resembles melting icicles with frozen droplets. This is because of the self-weight gravity induced viscous fluid during the P μ LSE manufacturing process. The surface of the diagonal strut exhibits a stacked structure topology, and randomly distributed hollow voids appear on the strut joints, as shown in Figure 5(b). These hollow voids are revealed by both SR- μ CT and optical microscopy. The octet-truss lattice structure can be represented by a typical unit cell, as shown in Figure 5(c).

The horizontal and diagonal struts were extracted for the surface morphology analysis. As shown in Figure 5(d), in front view, the top surface (1-1) exhibits an arc shape while the bottom surface (2-2) exhibits a straight line shape. As shown by the right elevation image in Figure 5(d), in contrast to the design, the manufactured sample's horizontal strut exhibits a non-circular cross section, which is drop-shaped and elliptical (3-3). It can be seen from the top and front views in Figure 5(e), the top surface (6-6) is smoother than the bottom surface (7-7), and right elevation features at different cross sections planes are exhibited by the cut planes (3-3), (4-4), and (5-5).

Figure 6 shows the defects formed in the strut joints of the octet-truss lattice structure. Figure 6(a) and (b) shows the reconstructed 3D distributions of the hollow pores and slice images of the defects formed at the strut joints, respectively.

Figure 7 demonstrates the image processing and fitting schemes on the strut cross section surface profile contour of

the octet-strut lattice structure. Firstly, horizontal and diagonal struts were extracted from the reconstructed tomography image. Subsequently, ten consecutive slices were selected for drawing the cross-sectional outline of the horizontal strut. The closed curves of different colors in Figure 7 represent the contours of different cross sections. Finally, the cross sections of the horizontal and diagonal struts were selected for fitting the average circle based on the least squares principle. The fitted curves are shown in black background in Figure 7(a) and (b). The closed curve is the cross-sectional profile of the reconstructed strut. The point in the figure indicates the centroid of the reconstructed strut cross-section, which is used to determine the center of the fitted circle. Finally, the radius of the fitted circle is selected

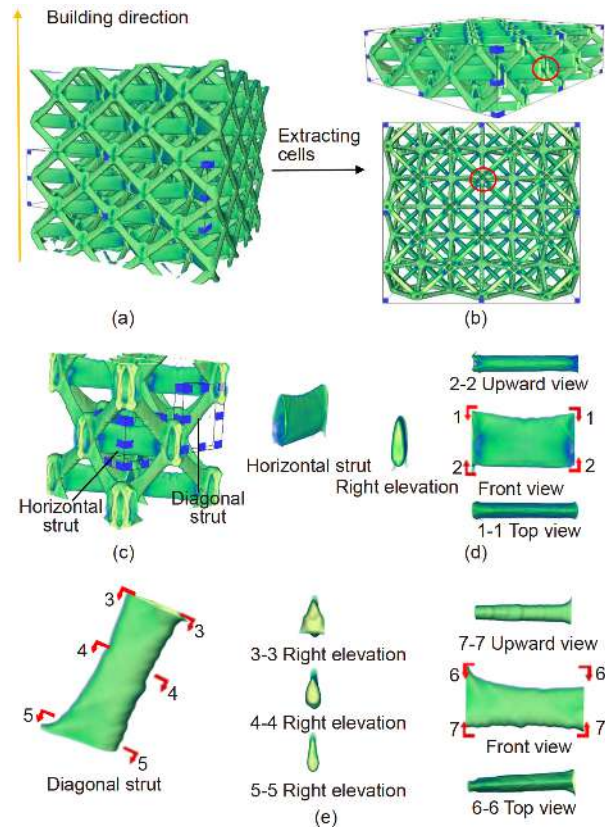


Figure 5 (Color online) Reconstructed sample 1 in 3D (a) and 2D (b); (c) reconstructed unit cell; reconstructed horizontal (d) and diagonal (e) strut and view of the horizontal strut in partial direction.

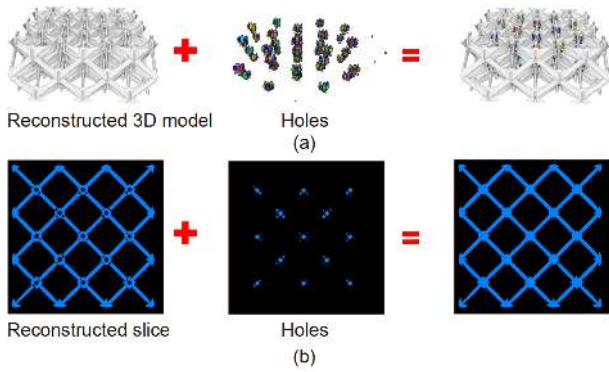


Figure 6 (Color online) Images of defects. (a) 3D tomography reconstructed distribution of defects at node locations; (b) slice image showing node defects.

based on the cross-sectional area equivalent principle of the reconstruction strut.

The probability density distribution of geometric defects is analyzed statistically based on the radius values data information of the cross sections of 17029 diagonal struts and 34087 horizontal struts. Figure 8(a) and (b) shows the radius distribution of the horizontal and diagonal struts, respectively. The average value u and standard deviation σ of the horizontal and diagonal strut radii are calculated separately. The superscripts “H” and “D” indicate the horizontal and the diagonal struts, respectively, and subscript “r” indicates the

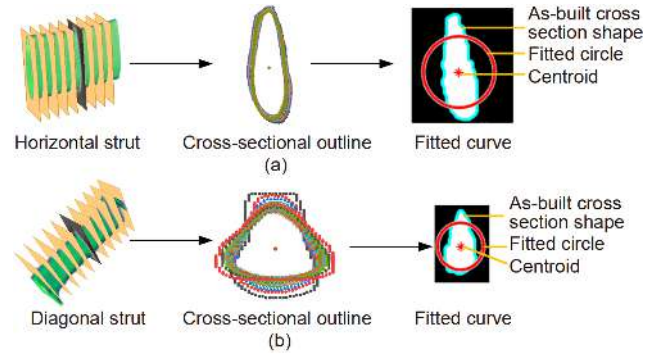


Figure 7 (Color online) Strut cross section surface profile topology fitting. (a) Horizontal strut fitted curve; (b) diagonal strut fitted curve

radius deviation information.

The radius distribution parameter in Figure 8 describes the geometrical defects of the strut. The standard deviation of the horizontal strut radius is $\sigma_r^H=24.0\%$. This is reflected in its cross-sectional variation (as shown in Figure 5(d)). The average value of the horizontal strut radius deviation is $u_r^H=-30.2\%$, and the radius of the horizontal strut is 30.2% smaller than the design radius, which is consistent with the result shown in Figure 8(c). The positive and negative signs on the value of the standard deviation of the strut’s radius indicate that the value is larger and smaller than the designed

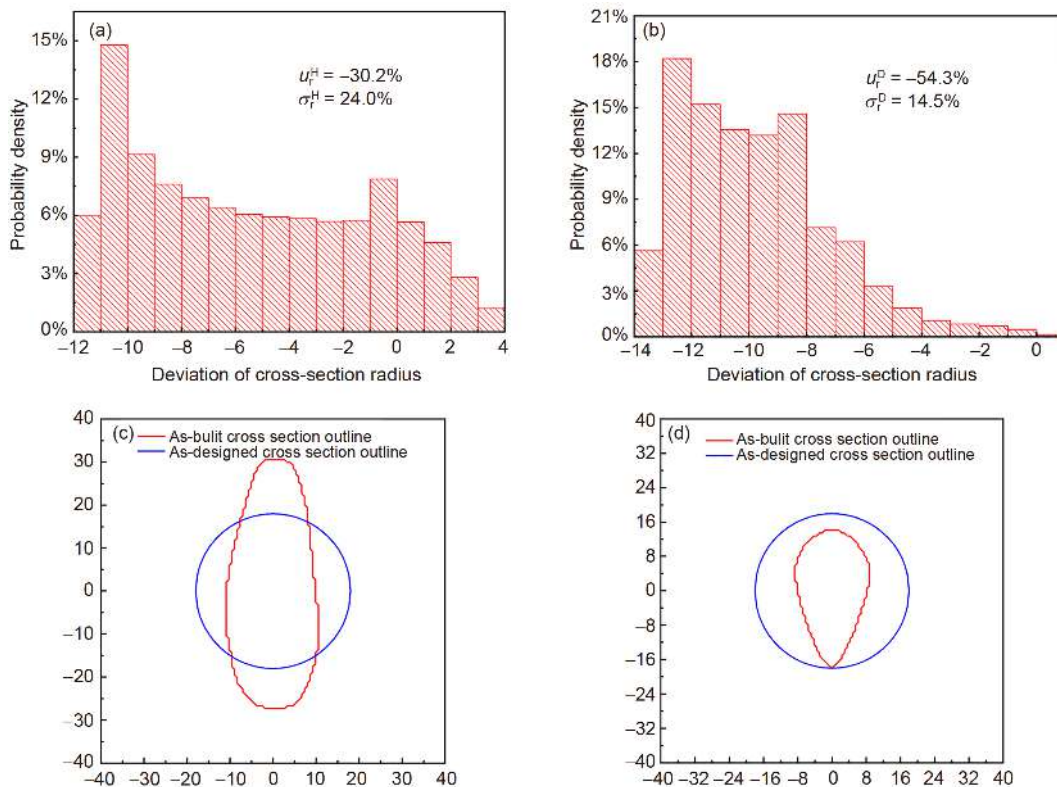


Figure 8 (Color online) Statistical distribution of strut radius for the octet-truss lattice structure. (a) Distribution of horizontal strut radii; (b) distribution of diagonal strut radii; cross-sectional outline of the (c) horizontal and (d) diagonal struts (μm).

radius, respectively. It was found that $\sigma_r^D=14.5\%$ and $u_r^D=-54.3\%$, are in good agreement with the result reported in Figure 8(d). The average radius of the horizontal strut (R_H) and the diagonal strut (R_D) are 18.3 and 12.3 μm , respectively, i.e., $R_D \approx 2/3 R_H$.

3.3.2 Tomography reconstruction and defect analysis for 3D re-entrant lattice structure

The reconstructed 3D models of the re-entrant lattice structure based on SR- μCT 3D imaging are shown in Figure 9(a), where several typical types of defects are identified, such as bulges, grooves, and stacks. Creeping-induced thickening is generated at the bottom layer (I) as a result of the influence of the building direction (along y axes) and structure's weight during the P μ LSE additive manufacturing process. The color depth indicates the level of the gray value, improving the image contrast. Figure 9(b) shows the tomography cross

section images in three orthogonal planes.

As shown in Figure 9(c), strut III is a vertical strut with a groove on the side surface and an arc shape on the upper surface. Strut IV can be further classified into two types of diagonal struts in re-entrant lattice structure induced by the weight: flat long and curved strut IV_2 and round thin and short strut IV_1 . The dislocation defects of the diagonal strut are shown by circles (marked 1); the groove on the surface of the vertical strut is shown by rectangle (marked 6); the curved pendant in the rectangle (marked 5) is all related to the building direction. Blocks adhere to the surface of the vertical strut, as shown by the circle (marked 2), owing to factors such as dust and impurities during the P μ LSE manufacturing process. The structure bears its own weight during the manufacturing process, causing diagonal strut to accumulate, as shown by the circle (marked 4). The unit cell V_1 in the dotted frame is inclined to the lower left. The result of unit cell V_1 and the result of optical microscopy are in good agreement. The unit cell V_2 is leant toward the lower right; the unit cell V_3 is tilted toward the upper left; the unit cell V_4 is inclined to the upper right. Figure 9(d) clearly shows the six views of the reconstructed 3D model.

Figure 10 shows the procedures followed for extracting strut cross-section geometrical information from the vertical and diagonal struts of the 3D re-entrant strut lattice structure. The cross-section of the strut was fitted with an ellipse. Firstly, the horizontal and diagonal struts are extracted from the reconstructed tomography models based on synchrotron X-ray 3D imaging. The contours of different cross sections are represented by closed curves of different colors, where ten consecutive cross sections are selected. Finally, the cross-section profiles of the horizontal and diagonal struts are selected for fitting the ellipse based on the least squares method, as shown by the black background in Figure 10(a)–(c). The cross-section profile of the reconstructed strut is represented by a closed curve. The dot represents the centroid of the reconstructed strut cross section and is used to determine the radius of the fitted ellipse (circle). The diagonal strut IV_1 is fitted with a circle. Finally, the radius of the fitted circle is determined by reconstructing the cross-sectional area of the strut.

In total, 943 diagonal struts IV_1 , 2079 diagonal struts IV_2 , and 1207 vertical struts are selected for the statistical analysis of the probability density of geometric defects, as shown in Figure 11. The observed statistical results are similar to the results reported in Figure 8, where the subscript “ T ” indicates the strut length deviation.

The side length of the vertical strut, diagonal strut IV_1 , and diagonal strut IV_2 are 37.4, 13.6, and 39.3 μm , respectively, which are smaller than the design values by 16.9%, 69.9%, and 12.7%, respectively. The average side length of the vertical strut is approximately equal to that of the diagonal strut IV_2 , and the average side length of the diagonal strut IV_2

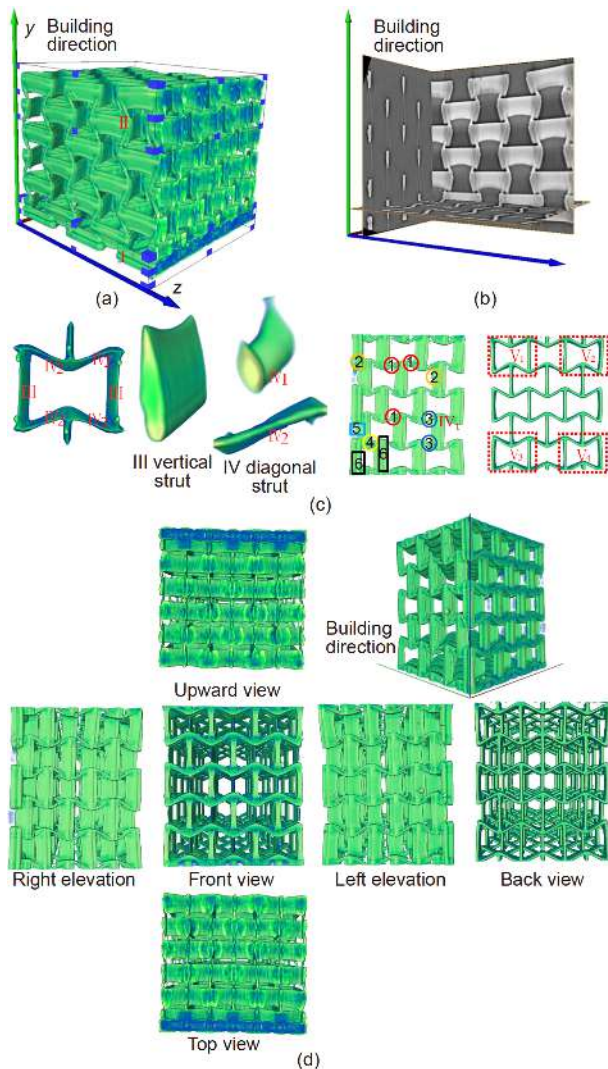


Figure 9 (Color online) Reconstructed model of sample 2. (a) Reconstructed 3D model; (b) tomography in the three orthogonal planes; (c) defects; (d) six views.

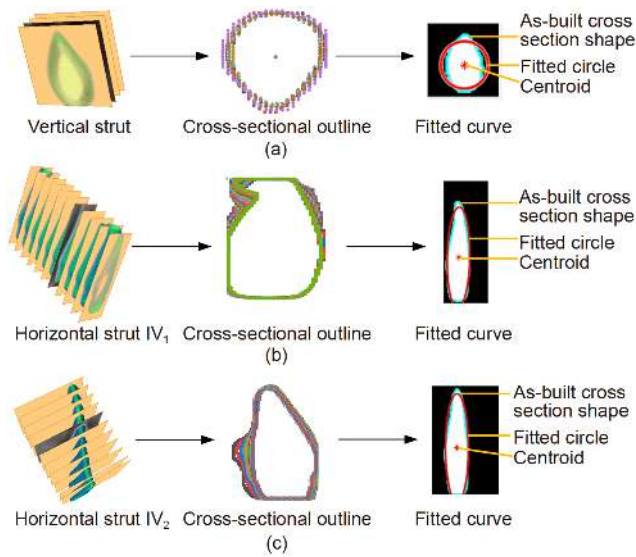


Figure 10 (Color online) Surface profile contour fitting for 3D re-entrant lattice. (a) Vertical strut fitted curve; (b)-(c) horizontal strut fitted curve.

is approximately 3 times greater than that of the diagonal strut IV_1 ($L_V \approx L_{IV_1} \approx 3L_{IV_2}$).

3.3.3 Defects classification for octet-truss and re-entrant lattice structures

The P μ LSE additive manufacturing process-induced imperfections of the lattice structures can be classified into the following categories in terms of defects, as shown in Figure 12. There are mainly two types of defects formed within the octet-truss lattice structure. Some hollow voids appear at the

nodes of the strut, and the diameter of the strut changes irregularly along the strut length. For the 3D re-entrant lattice structure, there are mainly six types of defects: irregular diameter variations, bulges, dislocations, grooves, accumulation, and torsion. Firstly, the generation of unwanted bubbles during the P μ LSE manufacturing process will lead to the formation of holes at the joints. Secondly, impurities in the raw materials will induce randomly distributed bulges on the surface of the struts. Finally, the deviation of the struts' diameter, the grooves on the strut surface, strut misalignment, material accumulation, and torsion deformations of the strut are all caused by their own weight during the solidification process.

The area of each cross section (sample 1) is identified and calculated using the MATLABR program to extract the effective radius, as shown in Figure 13(a). The underline and solid line represent the effective radius of the diagonal and horizontal struts, respectively. The design radius of the strut is shown by the double dotted line. Similarly, the effective side length of the strut of sample 2 is obtained by extracting the area of the cross section, as shown in Figure 13(b). The dotted line and underline are the effective side lengths of the diagonal strut; the double dotted line is the effective side length of the vertical strut; the solid line is the effective side length of the designed strut.

4 Conclusion

The defects of the 3D octet-truss and re-entrant lattice

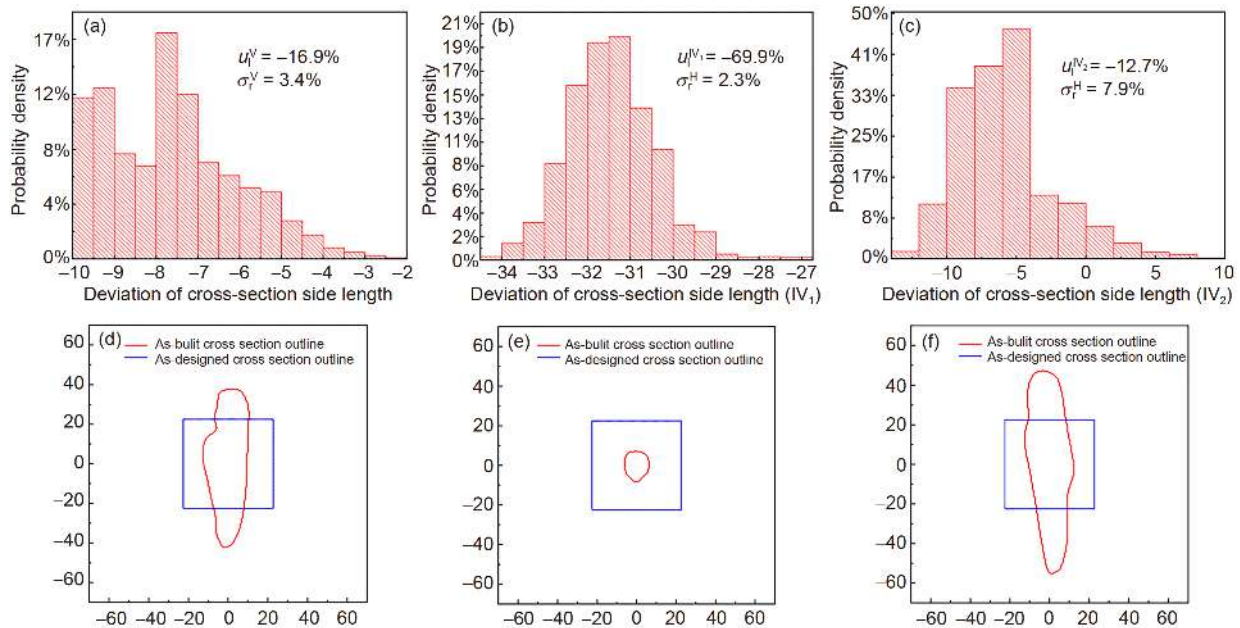


Figure 11 (Color online) Distribution of strut cross section for the re-entrant lattice structure. (a) Deviation of side length for vertical strut; (b) deviation of side length for diagonal strut IV_1 and (c) IV_2 ; (d) as-built and as-designed cross-sectional outline for vertical strut; (e) as-built and as-designed cross-sectional outline for diagonal strut IV_1 and (f) IV_2 .

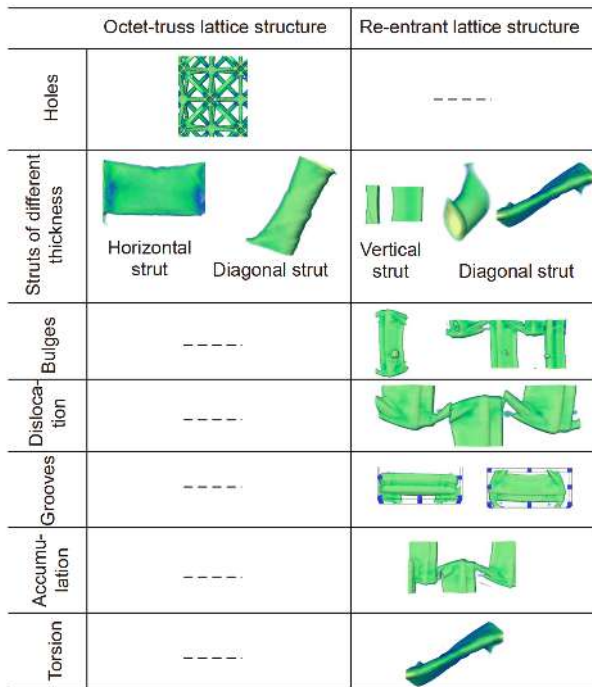


Figure 12 (Color online) Strut defect classification for samples 1 and 2.

structure manufactured with P μ LSE additive manufacturing technology were characterized using the SR- μ CT technique. The surface topography, internal defects, and cross-section profiles of the struts in 3D octet-truss and re-entrant structures were analyzed quantitatively, and the features of the defects were classified based on the geometrical statistic parameters of the struts along different directions and strut joints. The main findings of this study were the following.

(1) Two main defects were present in the octet-truss lattice structure: holes formed at the strut joints and deviations in the diameters of the struts. The average radius of the diagonal strut ($R_D=18.3\ \mu\text{m}$) was approximately 1.5 times greater than that of the horizontal strut ($R_H=12.3\ \mu\text{m}$), and the radius of the diagonal strut was approximately equal to the design radius ($R=18\ \mu\text{m}$).

(2) The main defects in the re-entrant lattice structure were the following: deviations in the diameters of the struts, bulges, dislocations, grooves, accumulation, and torsion. The average side length of the vertical strut ($L_V=37.4\ \mu\text{m}$) was approximately equal to that of the diagonal strut IV_2 ($L_{IV_2}=39.3\ \mu\text{m}$), and the average side length of the diagonal strut IV_2 was approximately 3 times greater than that of the diagonal strut IV_1 ($L_{IV_1}=13.6\ \mu\text{m}$). The average side length of the design strut ($L=45\ \mu\text{m}$) was approximately 1.2 times greater than that of the vertical strut.

(3) The generation of bubbles during the P μ LSE manufacturing process leads to the formation of holes at the joints and impurities in the raw materials cause bulges on the

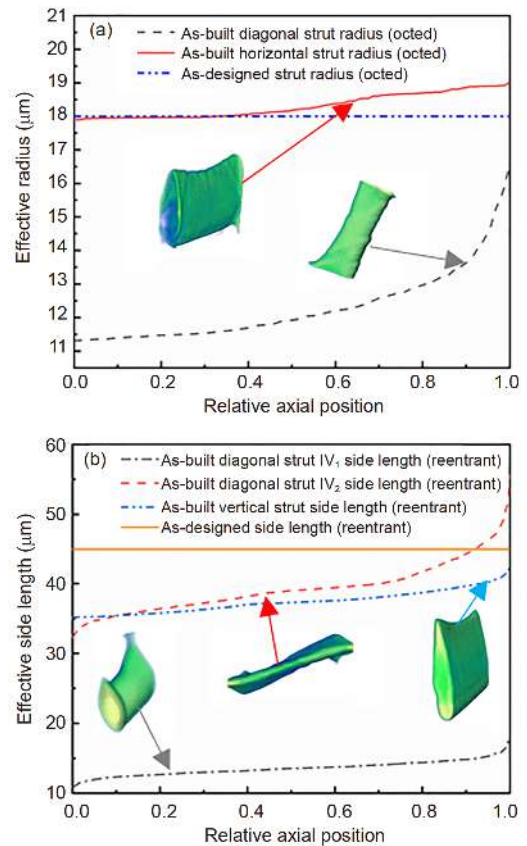


Figure 13 (Color online) (a) Radius of the octet-truss lattice structure and (b) side length of the re-entrant lattice structure.

surface of the struts. The variation in strut diameters, formation of grooves on the surface of the struts, accumulation of raw materials, and strut torsion and misalignment are all caused by their own weight during the solidification process. All of these defects are related to the building direction, the weight of the strut, bubble formation, and the introduction of dust and other impurities during the P μ LSE additive manufacturing process.

This work was supported by the National Natural Science Foundation of China (Grant Nos. 11702023, 11632010, 11972081), the Graduate Technological Innovation Project of Beijing Institute of Technology (Grant No. 2019CX20049). The authors would like to thank the BMF Precision Technology Co, Ltd. for supporting the micro/nano-scale 3D printing work.

- 1 Wu W, Hu W, Qian G, et al. Mechanical design and multifunctional applications of chiral mechanical metamaterials: A review. *Mater Des*, 2019, 180: 107950
- 2 Xiao D, Dong Z, Li Y, et al. Compression behavior of the graded metallic auxetic reentrant honeycomb: Experiment and finite element analysis. *Mater Sci Eng-A*, 2019, 758: 163–171
- 3 Wu W, Song X, Liang J, et al. Mechanical properties of anti-tetrachiral auxetic stents. *Composite Struct*, 2018, 185: 381–392
- 4 Bhargav A, Sanjairaj V, Rosa V, et al. Applications of additive manufacturing in dentistry: A review. *J Biomed Mater Res*, 2018, 106: 2058–2064
- 5 Camposeo A, Persano L, Farsari M, et al. Additive manufacturing: Applications and directions in photonics and optoelectronics. *Adv Opt*

- [Mater](#), 2019, 7: 1800419
- 6 Kim T B, Yue S, Zhang Z, et al. Additive manufactured porous titanium structures: Through-process quantification of pore and strut networks. [J Mater Processing Tech](#), 2014, 214: 2706–2715
 - 7 Kerckhofs G, Pyka G, Moesen M, et al. High-resolution microfocus X-ray computed tomography for 3D surface roughness measurements of additive manufactured porous materials. [Adv Eng Mater](#), 2013, 15: 153–158
 - 8 Song J, Gao L, Cao K, et al. Metal-coated hybrid meso-lattice composites and their mechanical characterizations. [Composite Struct](#), 2018, 203: 750–763
 - 9 Scarlett N V Y, Tyson P, Fraser D, et al. Synchrotron X-ray CT characterization of titanium parts fabricated by additive manufacturing. Part I. Morphology. [J Synchrotron Rad](#), 2016, 23: 1006–1014
 - 10 Scarlett N V Y, Tyson P, Fraser D, et al. Synchrotron X-ray CT characterization of titanium parts fabricated by additive manufacturing. Part II. Defects. [J Synchrotron Rad](#), 2016, 23: 1015–1023
 - 11 Uesugi M, Uesugi K, Takeuchi A, et al. Three-dimensional observation of carbonaceous chondrites by synchrotron radiation X-ray CT—Quantitative analysis and developments for the future sample return missions. [GeoChim CosmoChim Acta](#), 2013, 116: 17–32
 - 12 Fan X, He X, Nutor R K, et al. Effect of stress on crystallization behavior in a Fe-based amorphous ribbon: An *in situ* synchrotron radiation X-ray diffraction study. [J Magn Magn Mater](#), 2019, 469: 349–353
 - 13 Liu L, Kamm P, García-Moreno F, et al. Elastic and failure response of imperfect three-dimensional metallic lattices: The role of geometric defects induced by Selective Laser Melting. [J Mech Phys Solids](#), 2017, 107: 160–184
 - 14 Hu Y N, Wu S C, Song Z, et al. Effect of microstructural features on the failure behavior of hybrid laser welded AA7020. [Fatigue Fract Eng Mater Struct](#), 2018, 41: 2010–2023
 - 15 Wu S C, Hu Y N, Duan H, et al. On the fatigue performance of laser hybrid welded high Zn 7000 alloys for next generation railway components. [Int J Fatigue](#), 2016, 91: 1–10
 - 16 Wu S C, Xiao T Q, Withers P J. The imaging of failure in structural materials by synchrotron radiation X-ray microtomography. [Eng Fract Mech](#), 2017, 182: 127–156
 - 17 Wu Q, Vaziri A, Asl M E, et al. Lattice materials with pyramidal hierarchy: Systematic analysis and three dimensional failure mechanism maps. [J Mech Phys Solids](#), 2019, 125: 112–144
 - 18 Xu Y, Zhang H, Šavija B, et al. Deformation and fracture of 3D printed disordered lattice materials: Experiments and modeling. [Mater Design](#), 2019, 162: 143–153
 - 19 Carlton H D, Lind J, Messner M C, et al. Mapping local deformation behavior in single cell metal lattice structures. [Acta Mater](#), 2017, 129: 239–250
 - 20 Deshpande V S, Fleck N A, Ashby M F. Effective properties of the octet-truss lattice material. [J Mech Phys Solids](#), 2001, 49: 1747–1769
 - 21 Chen X Y, Tan H F. An effective length model for octet lattice. [Int J Mech Sci](#), 2018, 140: 279–287
 - 22 Wang X T, Wang B, Li X W, et al. Mechanical properties of 3D re-entrant auxetic cellular structures. [Int J Mech Sci](#), 2017, 131–132: 396–407
 - 23 Geng L, Wu W, Sun L, et al. Damage characterizations and simulation of selective laser melting fabricated 3D re-entrant lattices based on *in-situ* CT testing and geometric reconstruction. [Int J Mech Sci](#), 2019, 157–158: 231–242